

# INFRARED SPECTROSCOPY OF 15 RADIO GALAXIES AT $2 < z < 2.6$

FUMIHIDE IWAMURO<sup>1</sup>, KENTARO MOTOHARA<sup>2</sup>, TOSHINORI MAIHARA<sup>1</sup>, MASAHIKO KIMURA<sup>1</sup>, SHIGERU ETO<sup>1</sup>, TAKANORI SHIMA<sup>1</sup>, DAISAKU MOCHIDA<sup>1</sup>, SHINPEI WADA<sup>1</sup>, SATOKO IMAI<sup>1</sup>, AND KENTARO AOKI<sup>3</sup>

## ABSTRACT

Near-infrared spectra of 15 high-redshift radio galaxies (HzRGs) located at  $2 < z < 2.6$  were obtained by the OH Airglow Suppressor spectrograph mounted on the Subaru telescope. The UV-optical line ratio diagnostic diagrams indicate that half of the observed HzRGs have extended emission-line regions with low metal abundance, photoionized by a flat-continuum active galactic nucleus such as a quasar. We also found two probable correlations between radio and rest-optical parameters: (1) HzRGs with massive hosts tend to have a redder rest-optical continuum, and (2) HzRGs with smaller radio sizes also show a redder optical continuum. On the basis of the correlations, the nature of HzRGs at  $2 < z < 2.6$  is discussed.

*Subject headings:* galaxies: active — galaxies: formation — infrared: galaxies

## 1. INTRODUCTION

High redshift radio galaxies (HzRGs) have been studied as progenitors of the present massive galaxies. Their rest-UV morphologies usually show a clumpy structure with a bright nucleus (Rush et al. 1997; Pentericci et al. 1999), aligned with the axis of the radio sources in the so-called alignment effect. The major cause of the alignment effect is considered to be one of the following three mechanisms: (1) induced star formation by the passage of the radio jet (McCarthy et al.

1987; Chambers, Miley, & van Breugel 1987), (2) scattered light from a hidden active galactic nucleus (AGN: di Serego Alighieri et al. 1989; Cimatti et al. 1993), and (3) the nebular continuum (Dickson et al. 1995). These stellar, AGN, and nebular components make a nearly equal contribution to the UV continuum at the nucleus region of intermediate-redshift radio galaxies (Tadhunter et al. 2002). The rest-optical imaging of HzRGs shows the morphological evolution of host galaxies: multiple components spread over  $\sim 100$  kpc at  $z > 3$ , a single compact structure dominating at  $2 < z < 3$ , and an elliptical profile with a de Vaucouleurs  $r^{1/4}$  law formed at  $z \sim 1$  (van Breugel et al. 1998; Pentericci et al. 2001). The morphologies of the extended emission-line regions (EELRs) indicate the existence of a photoionization cone or shock-ionized region extended to several tens of kiloparsecs (Armus

<sup>1</sup>Department of Astronomy, Kyoto University, Kitashirakawa, Kyoto 606-8502, Japan.

<sup>2</sup>Institute of Astronomy, School of Science, University of Tokyo, 2-21-1 Osawa, Mitaka, Tokyo 181-0015, Japan.

<sup>3</sup>Subaru Telescope, National Astronomical Observatory of Japan, 650 North A'ohoku Place, University Park, Hilo, HI 96720.

et al. 1998; Motohara et al. 2000; Egami et al. 2003). They strongly support the unification model between radio loud quasars and radio galaxies.

The characteristics of HzRGs have been investigated by rest-UV spectroscopy. An HzRG with a smaller radio size has dense H I clouds surrounding the inner Ly $\alpha$  emitting region with a large turbulent velocity, probably because of the environmental effect on the radio size (van Ojik et al. 1997). The total (nucleus+EELR) ionization mechanism of UV emission lines is well explained by photoionization with a power-law index of  $\alpha = -1.0$  (Villar-Martín, Tadhunter, & Clark 1997), except for C II], which is enhanced by shock (De Breuck et al. 2000), and N V, which indicates an overabundance of nitrogen (Villar-Martín et al. 1999, 2001; Vernet et al. 2001). Concerning the physical conditions of the EELR, the existence of a metallicity gradient (Overzier et al. 2001) and the contribution of shock in the outer halo (Taniguchi et al. 2001) were reported, but the general mechanisms are still unknown. The contribution of the scattered AGN light to the UV continuum varies from object to object, between  $\sim 15\%$  and  $\sim 85\%$ , estimated by spectropolarimetry (Vernet et al. 2001).

On the other hand, rest-optical spectra of HzRGs show strong [O III] emission lines whose intensity has a correlation with the radio luminosity (Eales & Rawlings 1993, 1996; Iwamuro et al. 1996; Evans 1998). Reddened quasar light (or broad H $\alpha$ ) has also been detected from a few HzRGs (Larkin et al. 2000; Fosbury 2000). The emission line ratios of individual knots around the nucleus indicate that shock or starburst is the major ionization mechanism of these off-nuclear knots (Carson et al. 2001). Although the rest-optical spectra of HzRGs became observable within a reasonable exposure time by the newly built infrared instruments on the large telescopes, the published data are not sufficient to make statisti-

cal studies.

In this paper we present the rest-optical spectra of 15 HzRGs at  $2 < z < 2.6$  obtained by the OH Airglow Suppressor (OHS) spectrograph (Iwamuro et al. 2001) mounted on the Subaru telescope. The typical wavelength coverage of 3400–5400 Å includes major emission lines of AGNs, such as [O II]  $\lambda 3727$ , He II  $\lambda 4686$ , H $\beta$ , and [O III]  $\lambda 5007$ . In §2 we describe the observations and the reduction procedure of the 15 HzRGs. In §3, after we summarize the observed emission-line properties, we examine the major ionization mechanisms using UV-optical line ratio diagnostic diagrams. In §4 we discuss the nature of HzRGs on the basis of the probable correlations between several observed parameters, and we present our conclusions in §5.

Throughout the paper we adopt a cosmology with  $H_0 = 65 \text{ km s}^{-1} \text{ Mpc}^{-1}$ ,  $\Omega_M = 0.3$ , and  $\Omega_\Lambda = 0.7$ .

## 2. OBSERVATIONS AND DATA REDUCTION

A total of 15 well-known HzRGs with redshifts at  $2 < z < 2.6$  were observed during five test observation runs of the OHS mounted on the Subaru telescope in 2000 May, July, September, and December and 2001 August. For many targets, the rest-UV (and a part of the rest-optical) spectra and *Hubble Space Telescope* (*HST*) and Very Large Array images are available from the past literature. The rest-optical spectroscopy was carried out with the slit along the radio axis. The typical exposure sequence is 1000 s in four positions, in which the object is moved about  $10''$  along the slit by nodding the telescope after every exposure. The limiting magnitude is  $H=21.1$  (S/N=5 for 4000 s) at best with this sequence. A nearby Smithsonian Astrophysical Observatory (SAO) star with a spectral type of A or F was observed just after this exposure sequence and was used as a spectro-

scopic standard to remove telluric atmosphere absorption features and to correct the instrumental response. The  $J$ - (1.108–1.353  $\mu\text{m}$ ) and  $H$ -band (1.477–1.804  $\mu\text{m}$ ) spectra were simultaneously obtained with a spectral resolution of  $\sim 210$ . A slit width of  $1''$  corresponds to 9 pixels on a pixel scale of  $0''.111$  in the case of the optical secondary mirror of the telescope, which was generally used during these observations. Since the typical seeing size of  $0''.7$  is smaller than the slit width, we must take the morphology of the object within the slit into account when we consider the velocity structure of the emission lines. The observation log is summarized in Table 1.

All data reduction was performed using IRAF as follows:

1. Sky subtraction for a pair of spectroscopic images taken at different positions.
2. Flat-fielding using a standard  $H$ -band flat image (for correction of the local variations in the quantum efficiency).
3. Correction of unexpected hot pixels and cosmic-ray events.
4. Straightening of residual-airglow emission lines along column pixels.
5. Residual-airglow subtraction by fitting to each column excluding object positions (plus and minus images).
6. Shift-and-add of all images.
7. Correction of atmospheric absorption features and instrumental responses using the spectrum of the SAO star taken just after pointing at the object (where correction has already been applied to the hydrogenous absorption features and the intrinsic slope in the SAO spectrum).
8. Straightening of the object spectrum along line pixels.
9. Extraction of the object spectrum using a one-dimensional Gaussian mask with an FWHM of  $3''$ , except for TXS 0211–122, B3 0731+438, 4C +10.48, 4C +10.48 (FWHM of  $4''$ ), and 4C +23.56 (FWHM of  $2''$ ).

The resulting one-dimensional spectrum was calibrated using the photometric results of the  $H$ -band slitless imaging frame taken just before the spectroscopic observation. As a result, the average flux of the  $H$ -band spectrum corresponds to the  $H$ -band magnitude within an aperture diameter of  $2''.2$  (20 pixels).

### 3. RESULTS

#### 3.1. Line Fluxes and Continuum Levels

The final flux-calibrated spectra are presented in Figure 1. The right panels of this figure show the continuum profiles with 30 pixel smoothing, after fitting and subtraction of the emission lines with Gaussian functions. In this fitting procedure, each emission line is restored, fitted again, and subtracted individually to improve the estimation of the local continuum level (which is often affected by the residuals of neighboring emission lines). In order to achieve higher fitting accuracy, we assume a constant line ratio as well as the same FWHM and redshift for the following neon doublets: 3.32 for [Ne III]  $\lambda\lambda 3869, 3967$  and 2.74 for [Ne V]  $\lambda\lambda 3426, 3346$ , which are calculated by CLOUDY94 (Ferland 2000). Since both doublets are emitted by the transition from the  $^1D_2$  to  $^3P_{2,1}$  level, these ratios are expected to be invariable. For faint emission lines, we assume that the redshift is the same as that for [O III]  $\lambda 5007$  and that the FWHM is the instrumental value of  $\sim 75 \text{ \AA}$ . The emission line properties and the continuum levels are listed in Table 2.

## 3.2. Emission Line Ratios

### 3.2.1. UV-optical diagnostic diagrams

The UV line fluxes of C IV  $\lambda 1549$ , He II  $\lambda 1640$ , and C III]  $\lambda 1909$  are available for 13 out of 15 HzRGs from the past literature (Table 3). We combine these data with the optical line flux in Table 2 to examine the major ionization mechanisms of HzRGs. Figure 2 shows the UV-optical line ratio diagnostic diagrams. We calculated  $4 \times 4 \times 4$  photoionization sequences with CLOUDY94 (Ferland 2000) with power-law spectral indexes  $\alpha = 0.0, -0.5, -1.0$ , and  $-1.5$ , metal abundances  $Z = 0.1, 0.3, 1.0$ , and  $3.0 Z_{\odot}$ , and hydrogen densities  $N_{\text{H}} = 10, 100, 1000$ , and  $10^4 \text{ cm}^{-3}$ . The case of  $N_{\text{H}} = 1000 \text{ cm}^{-3}$  is plotted in Figure 2. Since the contribution of the hydrogen density to the emission line ratio is smaller than that of the other parameters, we can estimate the rough trend of  $\alpha$  and  $Z$  only from this case. The grid of the shock(+precursor) models (Dopita & Sutherland 1995; Allen et al. 1999; De Breuck et al. 2000) is also plotted in Figure 2.

The [O II]/[O III] vs. [O III]/ $\text{H}\beta$  diagram in Figure 2 is one of the most useful diagnostic diagrams for estimating the ionization parameter  $\log U$ , while the [O II]/[O III] vs. C IV/C III] and C IV/He II vs. [O III]/ $\text{H}\beta$  diagrams have advantages for estimating  $\alpha$  and  $Z$ , respectively. The degeneracy of the parameters can be solved by these diagrams, indicating  $\alpha \sim -0.5$ ,  $Z \sim 0.2 Z_{\odot}$ , and  $\log U \sim -2.2$  for our sample. On the other hand, the shock+precursor models are completely separated from the photoionization models in the [O II]/[O III] vs. He II/ $\text{H}\beta$  diagram. The majority of our samples seem to agree with the photoionization models; however, we cannot rule out the shock+precursor models for several objects only by this figure. The dust extinction, which may have a significant effect on the scatter of the data in the top left diagram of Figure 2, is expected to be small, be-

cause (1) the sizes of the EELRs are very large (10–30 kpc), and (2) the color of the rest-UV continuum (Röttgering et al. 1997; Vernet et al. 2001) is blue.

### 3.2.2. Best fit parameters

To determine the best-fit parameters for each object, we considered a nine-dimensional line ratio diagnostic diagram, which consists of all the UV/UV combinations of three UV lines (C IV, He II, and C III]: three combinations) and all the optical/optical combinations of four optical lines ([O II],  $\text{H}\beta$ , He II, and [O III]: six 6 combinations). Here we did not use any UV-optical line ratios, which may be affected by the differences of the instruments and the other observation parameters. In this nine-dimensional diagnostic diagram, the model grids as shown in Figure 2 were divided into 10 subgrids at even intervals. After the most probable subgrid giving the minimum  $\chi^2$  value was found, the nearest subgrids were divided into 10 sub-subgrids in order to search the most probable sub-subgrids again. The best-fit model with parameters was determined by iteration of the above calculation, as listed in Table 4. More than half of the objects can be explained by a photoionization model with a flat ionizing continuum and low metallicity, consistent with the distribution of the data in Figure 2. On the other hand, four objects are (also) in good agreement with the shock+precursor model, while three objects cannot be explained by a single-photoionization or shock+precursor model with a significant confidence level.

## 4. DISCUSSION

### 4.1. Correlations between Parameters

Before we discuss the nature of HzRGs, we review the correlations between the radio parameters (size, power, and spectral index) and the observed rest-optical parameters (continuum brightness, spectral index, [O III] lumi-

osity, and FWHM). The significance levels at which the null hypothesis of zero correlation is disproved are listed in Table 5 together with the correlation coefficients. Values marked with an asterisk in Table 5 indicate the probable correlations. In §4.2 we discuss these correlations individually.

## 4.2. Probable Correlations

### 4.2.1. Correlation between $P_{opt}$ and $\alpha_{opt}$

The correlation of the rest-optical continuum slope between [O II]  $\lambda 3727$  and [O III]  $\lambda 5007$  ( $\alpha_{opt}$ ; see Figure 1) with the continuum brightness at the rest-5007 Å wavelength ( $P_{opt}$ ) is shown in the left panel of Figure 3. Here  $P_{opt}$  roughly represents the mass of the host galaxy, because most of the continuum flux at the rest-5007 Å wavelength is expected to be of stellar origin (e.g., Fosbury 2000). With this taken into account, the  $P_{opt}$ - $\alpha_{opt}$  correlation indicates that a HzRG with a massive host has a redder optical color. For reference, the  $\alpha_{opt}$  values of the instantaneous starburst model change from  $-0.2$  (10 Myr) via  $-1.7$  (100 Myr) to  $-4.1$  (1 Gyr) without dust extinction, while the value of the scattered AGN light is expected to be  $\alpha_{opt} \sim 0$ .

### 4.2.2. Correlation between $D_{radio}$ and $\alpha_{opt}$

The correlations of  $\alpha_{opt}$  with the radio size ( $D_{radio}$ ) are shown in the right panel of Figure 3. A radio source with a smaller  $D_{radio}$  is usually thought to have a younger age of radio activity (Blundell & Rawlings 1999) or/and have dense gas clouds that interrupt the expansion of the radio jet (O’Dea 1998 and references therein). On the basis of the former idea, the older radio source should inhabit the bluer host galaxy, which seems difficult to explain. The latter idea indicates that the redder HzRG not only has a massive host (see §4.2.1) but also tends to be surrounded by dense gas clouds. Although the significance level of the  $D_{radio}$ - $P_{opt}$  correlation does not

reach a high confidence level (see Table 5), this inverse correlation does not conflict with this idea. The age of the radio source probably contributes to the scatter in these correlations.

## 4.3. Nature of HzRGs at $2 < z < 2.6$

From the UV-optical diagnostic diagrams and the probable correlations discussed above, the nature of HzRGs located at  $2 < z < 2.6$  is summarized as follows: The HzRGs with massive hosts show a redder optical color, indicating that the scattered light of the AGNs or massive blue stellar population does not make a significant contribution to their rest-optical spectra. These galaxies are also surrounded by dense gas clouds that interrupt the expansion of the radio jet. The radio activities do not have a large effect on these massive hosts, because the ages of the host galaxies expected from their red optical color ( $\gtrsim 100$  Myr) are older than the ages of typical radio activities ( $\sim 10$  Myr). On the other hand, the HzRGs with less massive hosts are not surrounded by dense gas clouds, corresponding to a larger radio size. The considerable contribution of the scattered light of the AGNs or massive blue stellar population makes their optical color blue. From the results of rest-UV spectropolarimetry reported by Vernet et al. (2001), the scattered light is the dominant contribution to these blue HzRGs with larger radio sizes (while massive red HzRGs such as B3 0731+438 and 4C +40.36 have a smaller contribution from scattered light). The ages of the host galaxies expected from their blue optical color ( $\lesssim 100$  Myr) are almost comparable to the ages of radio activities, implying that the current radio activities are closely related to the formation of the host galaxies.

The EELRs of HzRGs are usually photoionized by a flat-continuum AGN such as a quasar ( $\alpha \sim -0.5$ ), and the metal abundance is expected to be subsolar ( $Z \sim 0.2 Z_{\odot}$ ). In a few objects, shock+precursor is the dominant

ionization mechanism of the EELR, and three out of 13 objects cannot be explained by the single-ionization mechanism. A likely explanation is that the ionization mechanism of the EELR varies regionally, which requires further investigation into the spatial variation of the emission line ratios as well as the combination of photoionization and shock+precursor models (De Breuck et al. 2000; Moy & Rocca-Volmerange 2002) to fit the entire EELR spectra.

## 5. CONCLUSIONS

The nature of HzRGs located at  $2 < z < 2.6$  was investigated using their rest-optical spectra obtained by the OHS mounted on the Subaru telescope. We found two probable correlations between the radio and rest-optical parameters of the observed HzRGs as well as the characteristics of their ionization condition using UV-optical diagnostic diagrams.

1. *Correlation of  $P_{opt}$ - $\alpha_{opt}$ .*— HzRGs with massive hosts tend to have a redder optical continuum, indicating that the contribution of the scattered light of the AGNs or massive blue stellar population to the rest-optical spectra of these massive HzRGs is quite small. The contribution of the scattered light becomes larger for less massive objects, making their color blue.
2. *Correlation of  $D_{radio}$ - $\alpha_{opt}$ .*— HzRGs with smaller radio sizes also show a redder optical continuum. Together with the above correlation, HzRGs with massive hosts are surrounded by dense gas clouds, which interrupt the expansion of the radio jets. The radio activities do not have a large effect on these massive hosts, while they are closely related to the formation of the smaller host galaxies.
3. UV-optical diagnostic diagrams.— More

than half of the examined HzRGs are photoionized by a flat-continuum AGN such as a quasar ( $\alpha \sim -0.5$ ), which supports the unification model between HzRGs and quasars. In this case, the metal abundance of the EELR is subsolar ( $Z \sim 0.2 Z_{\odot}$ ). The shock+precursor models can explain a few cases, being expected to contribute to three other cases, which cannot be fitted by a single model.

These results were accomplished during test observation runs of the OHS using the Subaru telescope. We are therefore indebted to all members of the Subaru Observatory, National Astronomical Observatory of Japan.

## A. Notes on Particular Objects

Although most objects have a compact nucleus surrounded by an EELR, some of them show knot-like components or significant velocity structure. In this appendix, we show the two-dimensional spectra of these particular objects (Figures 4 and 5) and discuss their features individually.

### A.1. MRC 0156–252

This spectrum consists of a compact red continuum and [O III] emission lines. Since the position angle of the slit ( $50^\circ$ ) is almost the same as the position angle of the  $H$ -band morphology of this galaxy taken by *HST*/NICMOS (Pentericci et al. 2001), the origin of the tilt of the [O III] emission lines is not a morphological effect within the slit but a redshifted velocity structure of  $\sim 500 \text{ km s}^{-1}$ . This [O III] jet extends  $1''$  southwest along the slit from the nucleus. Our result is consistent with the dusty-quasar nature of this object reported by Eales & Rawlings (1996).

### A.2. MRC 0200+015

This galaxy has an [O III] knot separated  $2''.2$  south-southeast from the nucleus, which probably corresponds to the south radio lobe of this object (Carilli et al. 1997).

### A.3. MRC 0214+183

The detailed morphology of this galaxy is unknown. If the inclination of emission lines is due to the velocity difference, this galaxy has bipolar jets with velocities of approximately  $+400$  and  $-600 \text{ km s}^{-1}$  to the north and south directions, respectively.

### A.4. MRC 0406–244

This spectrum shows multiple components of emission lines with a single continuum. The main body of this galaxy consists of two components in the optical and near-infrared images taken by *HST* (Rush et al. 1997; Pentericci et al. 2001), which correspond to components  $a_1$  and  $a_2$  in Figure 5. Component  $a_1$  is located at the ridge of the continuum emission of the host galaxy. Component  $a_2$  is a redshifted knot with a velocity of  $\sim 500 \text{ km s}^{-1}$ . The other two knots (components  $b$  and  $c$  in Figure 5) are parts of the outer EELR of this galaxy.

### A.5. B3 0731+438

The knotlike structure of the [O III] emission lines are a part of the ionization cone of this galaxy (Motohara et al. 2000). The velocity offset of this component is not real but due to the morphological structure within the slit. Most of the line emission comes from the southern ionization cone, where a faint blue continuum is marginally detected, indicating the existence of a blue stellar population rather than scattered AGN light (Vernet et al. 2001).

### A.6. TXS 0828+193

This galaxy has the most complicated spectrum in our sample. The [O III] emission lines consist of three components, which correspond to the knots  $b$ ,  $a$ , and  $c$  in Figure 5 of Steinbring, Crampton, & Hutchings (2002) from top to bottom. We cannot confirm a velocity structure of [O III] emission lines, because it is probably caused by a morphological effect within the slit. The continuum

emission shows two components: one is a bluer northern component including [O III] knot b, and the other is a redder southern component including [O III] knot a. These results strongly support the idea that the northern component is the scattered light from a hidden AGN in the southern host galaxy (Pentericci et al. 1999; Steinbring et al. 2002).

#### **A.7. 4C -00.62**

The EELR of this galaxy extends along the radio jet to the west-southwest direction (Pentericci et al. 2000).

#### **A.8. 4C +40.36**

This spectrum shows the most broad [O III] emission-line width in our sample, which is more than  $1400 \text{ km s}^{-1}$  after the instrumental contribution is subtracted. The distortion of emission lines is probably due to the morphological structure of this object (Egami et al. 2003).



## REFERENCES

- Allen, M. G., Dopita, M. A., Tsvetanov, Z. I., & Sutherland, R. S. 1999, *ApJ*, 511, 686
- Armus, L., Soifer, B. T., Murphy, T. W., Neugebauer, G., Evans, A. S., & Matthews, K. 1998, *ApJ*, 495, 276
- Blundell, K. M. & Rawlings, S. 1999, *Nature*, 399, 330
- Carilli, C. L., Röttgering, H. J. A., van Ojik, R., Miley, G. K., & van Breugel, W. J. M. 1997, *ApJS*, 109, 1
- Carson, J. E. et al. 2001, *ApJ*, 563, 63
- Chambers, K. C., Miley, G. K., & van Breugel, W. 1987, *Nature*, 329, 604
- Cimatti, A., di Serego-Alighieri, S., Fosbury, R. A. E., Salvati, M., & Taylor, D. 1993, *MNRAS*, 264, 421
- De Breuck, C., Röttgering, H., Miley, G., van Breugel, W., & Best, P. 2000, *A&A*, 362, 519
- Dickson, R., Tadhunter, C., Shaw, M., Clark, N., & Morganti, R. 1995, *MNRAS*, 273, L29
- di Serego Alighieri, S., Fosbury, R. A. E., Tadhunter, C. N., & Quinn, P. J. 1989, *Nature*, 341, 307
- Dopita, M. A. & Sutherland, R. S. 1995, *ApJ*, 455, 468
- Eales, S. A. & Rawlings, S. 1993, *ApJ*, 411, 67
- Eales, S. A. & Rawlings, S. 1996, *ApJ*, 460, 68
- Egami, E., Armus, L., Neugebauer, G., Murphy, T. W., Soifer, B. T., Matthews, K., & Evans, A. S. 2003, *AJ*, 125, 1038
- Evans, A. S. 1998, *ApJ*, 498, 553
- Ferland, G. J. 2000, *Revista Mexicana de Astronomia y Astrofisica Conference Series*, 9, 153
- Fosbury, R. A. 2000, *Proc. SPIE*, 4005, 76
- Iwamuro, F., Oya, S., Tsukamoto, H., & Maihara, T. 1996, *ApJ*, 466, L67
- Iwamuro, F., Motohara, K., Maihara, T., Hata, R., & Harashima, T. 2001, *PASJ*, 53, 355
- Larkin, J. E. et al. 2000, *ApJ*, 533, L61
- McCarthy, P. J., van Breugel, W., Spinrad, H., & Djorgovski, S. 1987, *ApJ*, 321, L29
- Motohara, K. et al. 2000, *PASJ*, 52, 33
- Moy, E. & Rocca-Volmerange, B. 2002, *A&A*, 383, 46
- O'Dea, C. P. 1998, *PASP*, 110, 493
- Overzier, R. A., Röttgering, H. J. A., Kurk, J. D., & De Breuck, C. 2001, *A&A*, 367, L5
- Pentericci, L., Röttgering, H. J. A., Miley, G. K., McCarthy, P., Spinrad, H., van Breugel, W. J. M., & Macchetto, F. 1999, *A&A*, 341, 329
- Pentericci, L., Van Reeve, W., Carilli, C. L., Röttgering, H. J. A., & Miley, G. K. 2000, *A&AS*, 145, 121
- Pentericci, L., McCarthy, P. J., Röttgering, H. J. A., Miley, G. K., van Breugel, W. J. M., & Fosbury, R. 2001, *ApJS*, 135, 63
- Röttgering, H. J. A., van Ojik, R., Miley, G. K., Chambers, K. C., van Breugel, W. J. M., & de Koff, S. 1997, *A&A*, 326, 505
- Rush, B., McCarthy, P. J., Athreya, R. M., & Persson, S. E. 1997, *ApJ*, 484, 163

- Steinbring, E., Crampton, D., & Hutchings, J. B. 2002, *ApJ*, 569, 611
- Tadhunter, C., Dickson, R., Morganti, R., Robinson, T. G., Wills, K., Villar-Martin, M., & Hughes, M. 2002, *MNRAS*, 330, 977
- Taniguchi, Y. et al. 2001, *ApJ*, 559, L9
- van Breugel, W. J. M., Stanford, S. A., Spinrad, H., Stern, D., & Graham, J. R. 1998, *ApJ*, 502, 614
- van Ojik, R., Röttgering, H. J. A., Miley, G. K., & Hunstead, R. W. 1997, *A&A*, 317, 358
- Vernet, J., Fosbury, R. A. E., Villar-Martín, M., Cohen, M. H., Cimatti, A., di Serego Alighieri, S., & Goodrich, R. W. 2001, *A&A*, 366, 7
- Villar-Martin, M., Tadhunter, C., & Clark, N. 1997, *A&A*, 323, 21
- Villar-Martín, M., Fosbury, R. A. E., Binette, L., Tadhunter, C. N., & Rocca-Volmerange, B. 1999, *A&A*, 351, 47
- Villar-Martín, M., Fosbury, R., Vernet, J., Cohen, M., Cimatti, A., & di Serego Alighieri, S. 2001, *Astrophysics and Space Science Supplement*, 277, 571

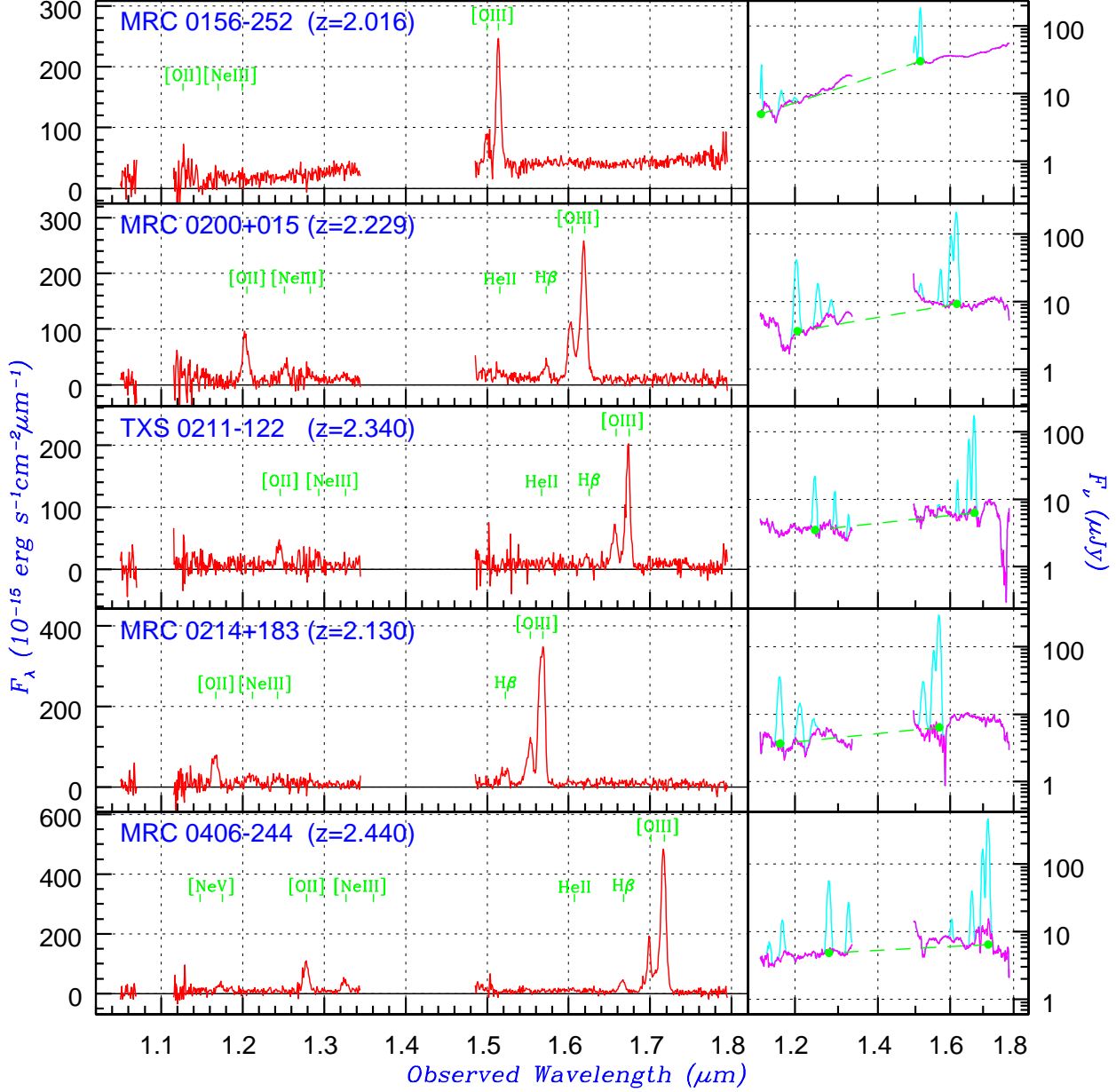


Fig. 1.— One-dimensional spectra of  $2 < z < 2.6$  HzRGs. The flux is calibrated using the  $H$ -band magnitude with a  $2''.2$  diameter aperture (see section 2). The right panels show the continuum shape smoothed over 30 pixels (*thick lines*) after subtraction of the emission lines (*thin lines*). The continuum levels at  $[\text{O II}] \lambda 3727$  and  $[\text{O III}] \lambda 5007$  (listed in Table 2) are indicated by filled circles and connected with dashed lines. [See the electronic edition of the *Journal* for a color version of this figure.]

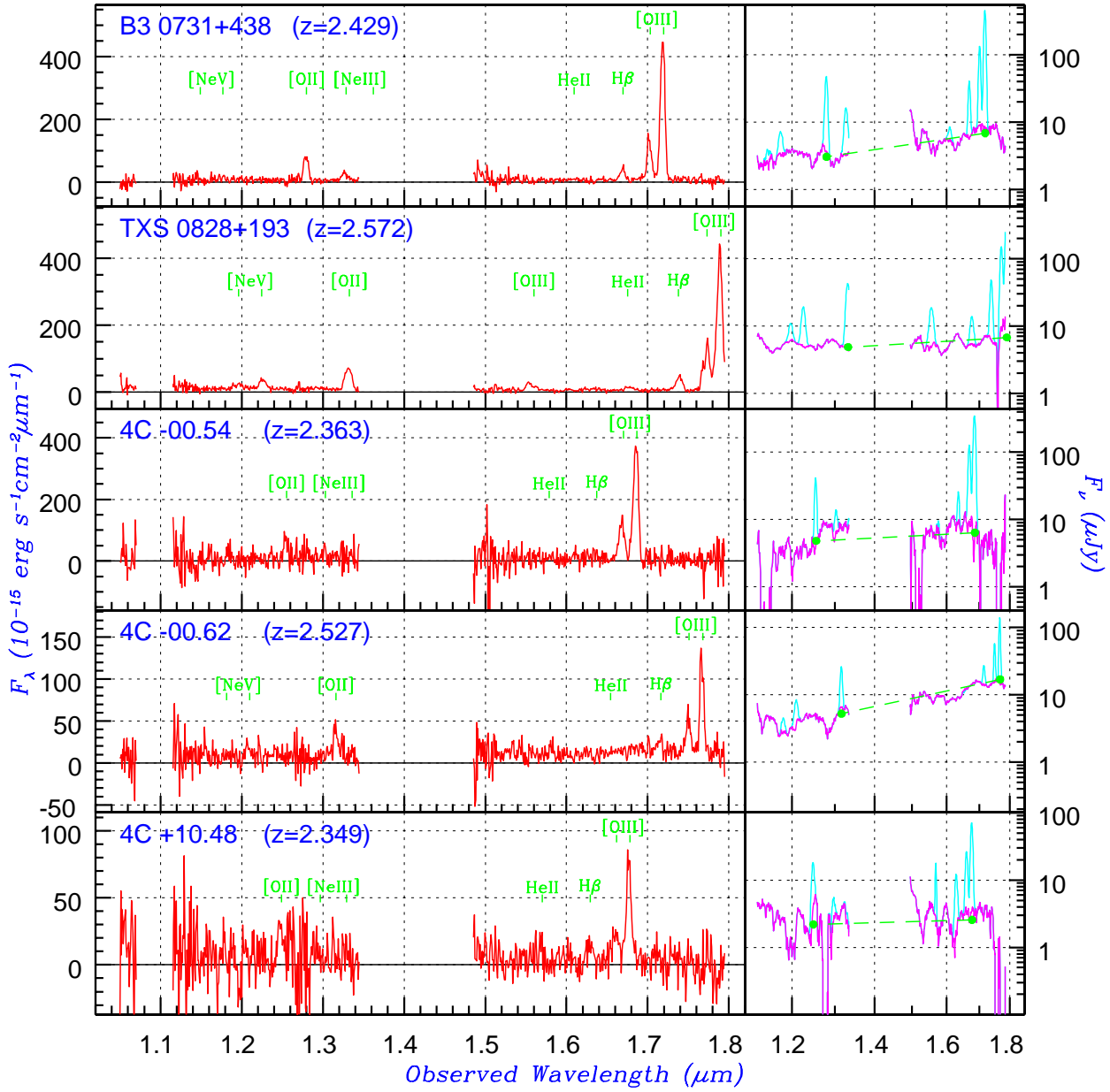


Fig. 1.— (continued)

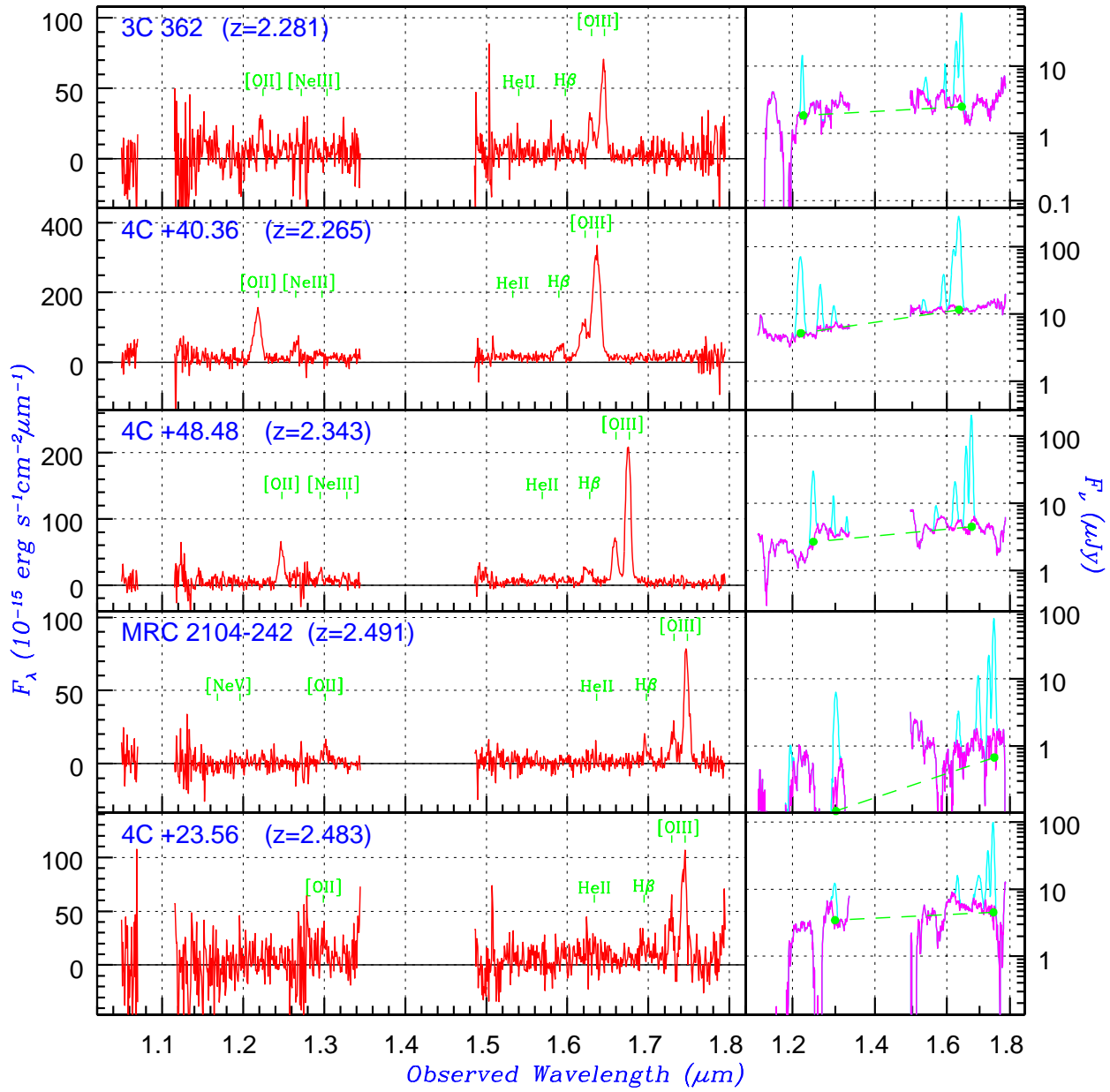


Fig. 1.— (continued)

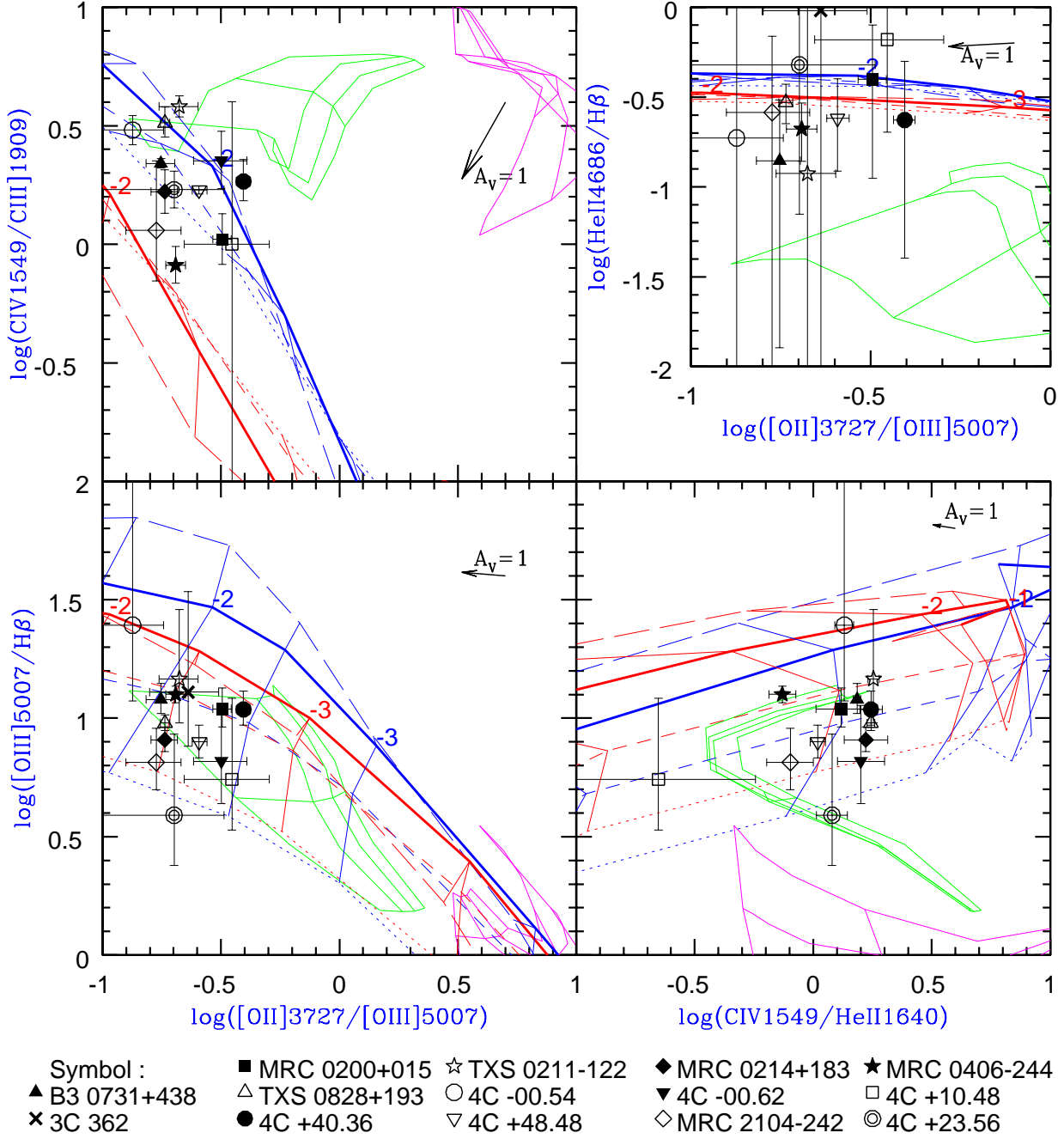


Fig. 2.— Optical-UV line ratio diagnostic diagrams. Plots of  $2 \times 4$  photoionization sequences with power-law spectral indexes of  $-0.5$  (blue lines) and  $-1.0$  (red lines) and with metal abundance  $Z = 0.1$  (dotted lines),  $0.3$  (dashed lines),  $1.0$  (thick solid lines), and  $3.0 Z_{\odot}$  (long-dashed lines) are plotted with a  $0.5$  dex step of  $\log U$ . The hydrogen density for these models is the fixed value of  $N_{\text{H}} = 1000 \text{ cm}^{-3}$ . Shock (magenta lines) and shock+precursor (green lines) models are shown with a grid of  $B/\sqrt{n} = 0, 1, 2,$  and  $4 \mu\text{G cm}^{3/2}$  and  $v = 200, 300,$  and  $500 \text{ km s}^{-1}$ .

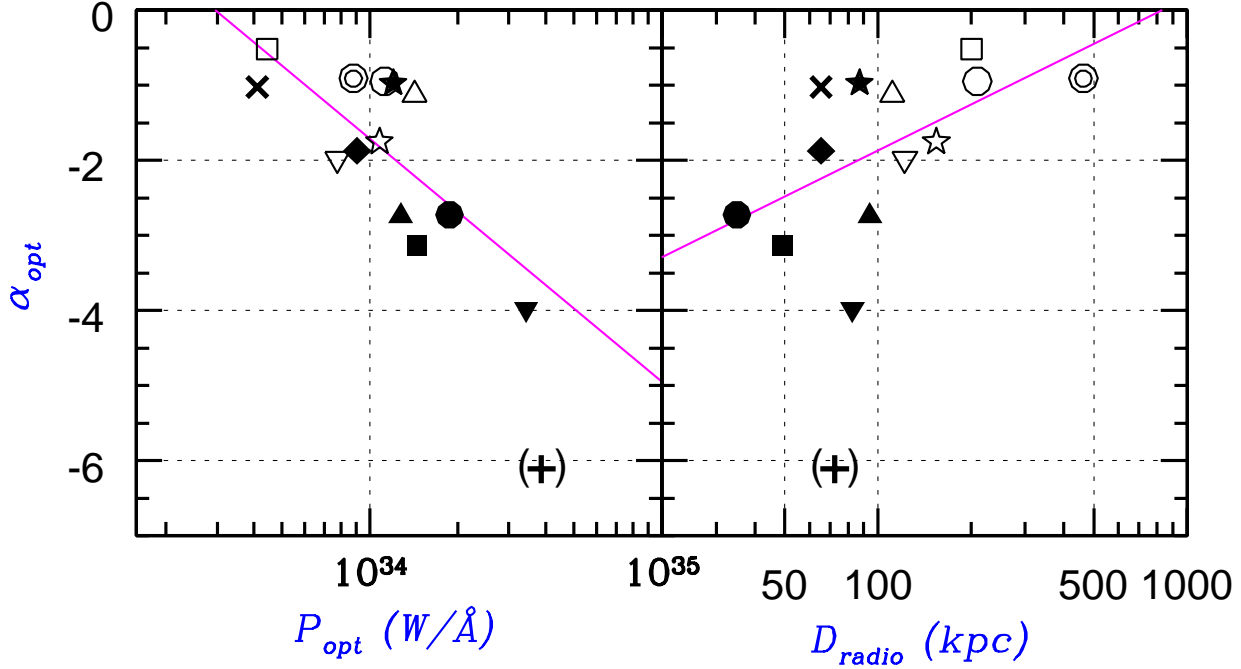


Fig. 3.— Probable correlations between parameters. The symbols are the same as in Figure 2, while solid lines correspond to the results of linear least-squares fits. MRC 0156–252 (*plus symbol with brackets*) is plotted together with the other samples only for comparison and is not included in the estimation of the correlation significance. MRC 2104–242 is also excluded from the estimation of the correlation significance with  $\alpha_{opt}$  (see footnotes of Table 5). [*See the electronic edition of the Journal for a color version of this figure.*]

Fig. 4.— Two-dimensional spectra of particular objects. The observed spectra have discontinuous spectral ranges because of the instrumental throughput of OHS: 1.05–1.08, 1.11–1.35, and 1.48–1.80  $\mu\text{m}$  from left to right. [*See the electronic edition of the Journal for a color version of this figure.*]

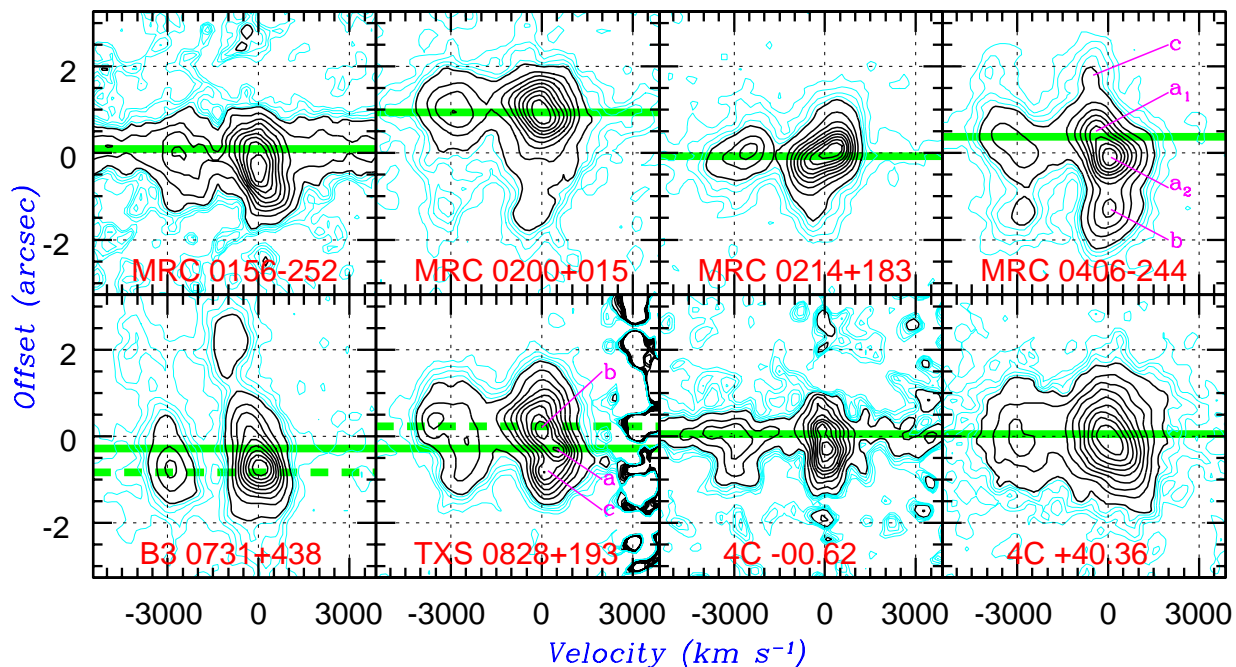


Fig. 5.— Two-dimensional emission line structures of the  $[\text{O III}] \lambda\lambda 4959, 5007$  shown in Figure 4. The spectra have been smoothed with a Gaussian of 1 pixel ( $0''.111$  or  $8.7 \text{ \AA}$ ). Thick contours are linearly spaced from 10% to 90% of the peak flux, with an interval of 10%, while the thin contours denote 2%, 4%, 6%, and 8% levels. Solid horizontal lines show the position of the continuum emission of the host galaxies. Dashed horizontal lines in B3 0731+438 and TXS 0828+193 correspond to the position of the faint blue continuum (see Appendix). [*See the electronic edition of the Journal for a color version of this figure.*]



TABLE 1  
LOG OF OBSERVATIONS

Common Name	IAU Name	$H$ -mag <sup>a</sup>	Redshift	Date	Exposure Time (s)	Slit P.A. (degree)	Seeing (arcsec)
MRC 0156–252	0156–252	18.45	2.016	2000 Sep 15	4000	+50	0.6
MRC 0200+015	0200+015	19.26	2.229	2001 Jul 31	3000	–24	0.6
TXS 0211–122	0211–122	19.82	2.340	2000 Dec 18	4000	–78	0.7
MRC 0214+183	0214+183	19.19	2.130	2001 Aug 01	5000	–2	0.6
MRC 0406–244	0406–244	19.11	2.440	2000 Sep 15	6000	–48	0.6
B3 0731+438	0731+438	19.35	2.429	2000 Dec 17	4000	+18	0.6
TXS 0828+193	0828+193	19.40	2.572	2000 Dec 18	4000	+38	0.7
4C –00.54	1410–001	19.48	2.363	2000 May 20	3000	–47	0.6
4C –00.62	1558–003	19.69	2.527	2000 May 21	4000	+76	0.6
4C +10.48	1707+105	20.72	2.349	2001 Aug 01	4000	+52	0.8
3C 362	1744+183	20.67	2.281	2000 May 22	3000	+51	0.7
4C +40.36	1809+407	18.93	2.265	2000 May 23	3200	+82	0.8
4C +48.48	1931+480	19.86	2.343	2000 Jul 24	4000	+29	1.0
MRC 2104–242	2104–242	21.13	2.491	2000 Sep 14	4000	+17	0.8
4C +23.56	2105+233	20.22	2.483	2000 Jul 24	1000 <sup>b</sup>	+51	0.8

<sup>a</sup>Observed  $H$ -band magnitudes by OHS imaging observations with a 2''-diameter aperture. Typical photometric errors are 0.05 mag.

<sup>b</sup>The exposure sequence was terminated by instrument trouble with the telescope.

TABLE 2  
EMISSION LINE PROPERTIES AND CONTINUUM LEVELS

Common Name	Lines	Wavelength ( $\mu\text{m}$ )	Redshift <sup>a</sup>	Line Flux <sup>b</sup>	Equivalent Width <sup>c</sup> ( $\text{\AA}$ )	FWHM <sup>a,d</sup> ( $\text{km s}^{-1}$ )	Continuum Level <sup>e</sup>
MRC 0156–252	[O III] $\lambda$ 5007	1.5139	2.0237	$13.02 \pm 0.52$	109	$1213^{+82}_{-36}$	39.57
	[Ne III] $\lambda$ 3869	1.1699	...	$0.84 \pm 0.52$	20	...	13.94
	[O II] $\lambda$ 3727	1.1276	2.0256	$1.55 \pm 0.76$	44	$784^{+917}_{-329}$	11.75
MRC 0200+015	[O III] $\lambda$ 5007	1.6184	2.2322	$21.60 \pm 0.34$	630	$1628^{+32}_{-25}$	10.60
	H $\beta$	1.5722	2.2342	$1.97 \pm 0.34$	51	$1402^{+303}_{-234}$	12.00
	He II $\lambda$ 4686	1.5157	2.2346	$0.78 \pm 0.52$	17	$1492^{+6938}_{-561}$	13.86
	[Ne III] $\lambda$ 3869	1.2522	2.2365	$2.60 \pm 0.42$	97	$2189^{+468}_{-368}$	8.27
	[O II] $\lambda$ 3727	1.2033	2.2286	$6.92 \pm 0.52$	282	$2045^{+188}_{-167}$	7.59
TXS 0211–122	[O III] $\lambda$ 5007	1.6727	2.3407	$12.18 \pm 0.31$	545	$1164^{+21}_{-59}$	6.69
	H $\beta$	1.6220	2.3367	$0.83 \pm 0.40$	35	$889^{+681}_{-316}$	7.10
	He II $\lambda$ 4686	1.5655	...	$0.10 \pm 0.36$	4	...	7.66
	[Ne III] $\lambda$ 3869	1.2922	2.3399	$0.91 \pm 0.43$	42	$1092^{+952}_{-343}$	6.40
	[O II] $\lambda$ 3727	1.2449	2.3402	$2.57 \pm 0.42$	114	$1622^{+337}_{-253}$	6.74
MRC 0214+183	[O III] $\lambda$ 5007	1.5671	2.1299	$32.69 \pm 0.32$	1346	$1673^{+20}_{-16}$	7.76
	H $\beta$	1.5221	2.1313	$4.03 \pm 0.44$	187	$2272^{+307}_{-248}$	6.88
	[Ne III] $\lambda$ 3869	1.2109	2.1299	$2.44 \pm 0.51$	91	$2571^{+774}_{-393}$	8.55
	[O II] $\lambda$ 3727	1.1663	2.1293	$5.99 \pm 0.71$	237	$2019^{+292}_{-238}$	8.06
MRC 0406–244	[O III] $\lambda$ 5007	1.7161	2.4274	$37.79 \pm 0.34$	1677	$1340^{+44}_{-5}$	6.57
	H $\beta$	1.6658	2.4269	$3.00 \pm 0.21$	121	$1389^{+116}_{-103}$	7.23
	He II $\lambda$ 4686	1.6046	2.4243	$0.63 \pm 0.18$	24	$1208^{+829}_{-360}$	7.60
	[Ne III] $\lambda$ 3869	1.3252	2.4251	$2.89 \pm 0.39$	95	$1659^{+244}_{-207}$	8.93
	[O II] $\lambda$ 3727	1.2778	2.4285	$7.69 \pm 0.67$	252	$1786^{+166}_{-149}$	8.91
	[Ne V] $\lambda$ 3426	1.1723	2.4216	$1.59 \pm 0.29$	52	$1661^{+478}_{-264}$	9.01
B3 0731+438	[O III] $\lambda$ 5007	1.7183	2.4319	$31.36 \pm 0.43$	1319	$1135^{+22}_{-14}$	6.93
	H $\beta$	1.6690	2.4335	$2.61 \pm 0.34$	110	$1179^{+183}_{-155}$	6.94
	He II $\lambda$ 4686	1.6097	2.4352	$0.37 \pm 0.33$	17	$1907^{+7437}_{-1022}$	6.25
	[Ne III] $\lambda$ 3869	1.3269	2.4296	$2.15 \pm 0.43$	125	$2059^{+585}_{-418}$	5.01
	[O II] $\lambda$ 3727	1.2792	2.4324	$5.54 \pm 0.69$	290	$1508^{+188}_{-161}$	5.56
	[Ne V] $\lambda$ 3426	1.1751	2.4300	$0.82 \pm 0.52$	36	$2334^{+3431}_{-959}$	6.72
TXS 0828+193	[O III] $\lambda$ 5007	1.7888	2.5726	$35.64 \pm 0.36$	1571	$1434^{+53}_{-6}$	6.35
	H $\beta$	1.7388	2.5770	$3.74 \pm 0.24$	165	$1448^{+112}_{-100}$	6.32
	He II $\lambda$ 4686	1.6773	2.5793	$1.10 \pm 0.20$	53	$2060^{+495}_{-363}$	5.84
	H $\gamma$ + [O III]	1.5553	2.5746 <sup>f</sup>	$2.35 \pm 0.24$	105	$2465^{+314}_{-262}$	6.24
	[O II] $\lambda$ 3727	1.3314	2.5723	$6.55 \pm 0.23$	223	$2134^{+86}_{-81}$	8.22
	[Ne V] $\lambda$ 3426	1.2257	2.5776	$2.85 \pm 0.30$	76	$2302^{+245}_{-318}$	10.43
4C –00.54	[O III] $\lambda$ 5007	1.6852	2.3657	$28.28 \pm 0.96$	1251	$1298^{+53}_{-48}$	6.72

TABLE 2—Continued

Common Name	Lines	Wavelength ( $\mu\text{m}$ )	Redshift <sup>a</sup>	Line Flux <sup>b</sup>	Equivalent Width <sup>c</sup> ( $\text{\AA}$ )	FWHM <sup>a,d</sup> ( $\text{km s}^{-1}$ )	Continuum Level <sup>e</sup>
	H $\beta$	1.6356	2.3647	1.15 $\pm$ 1.16	42	1021 <sup>+9188</sup> <sub>-494</sub>	8.10
	He II $\lambda$ 4686	1.5772	...	0.21 $\pm$ 1.48	8	...	8.29
	[Ne III] $\lambda$ 3869	1.3022	...	1.10 $\pm$ 1.34	29	...	11.28
	[O II] $\lambda$ 3727	1.2540	2.3648	3.79 $\pm$ 1.15	123	1166 <sup>+515</sup> <sub>-311</sub>	9.18
4C -00.62	[O III] $\lambda$ 5007	1.7666	2.5282	6.54 $\pm$ 0.59	114	856 <sup>+87</sup> <sub>-72</sub>	16.29
	H $\beta$	1.7153	2.5287	0.99 $\pm$ 0.36	19	1185 <sup>+775</sup> <sub>-374</sub>	14.47
	He II $\lambda$ 4686	1.6533	...	0.00 $\pm$ 0.50	0	...	12.67
	[O II] $\lambda$ 3727	1.3155	2.5295	2.07 $\pm$ 0.35	65	1301 <sup>+344</sup> <sub>-240</sub>	9.08
	[Ne V] $\lambda$ 3426	1.2088	...	0.86 $\pm$ 0.41	30	...	8.13
4C +10.48	[O III] $\lambda$ 5007	1.6766	2.3486	5.62 $\pm$ 0.42	615	1309 <sup>+142</sup> <sub>-105</sub>	2.73
	H $\beta$	1.6288	2.3508	1.02 $\pm$ 0.52	91	1466 <sup>+1041</sup> <sub>-550</sub>	3.34
	He II $\lambda$ 4686	1.5685	2.3472	0.67 $\pm$ 0.36	55	647 <sup>+479</sup> <sub>-218</sub>	3.65
	[Ne III] $\lambda$ 3869	1.2956	...	0.43 $\pm$ 0.66	33	...	3.95
	[O II] $\lambda$ 3727	1.2476	2.3475	1.98 $\pm$ 0.64	140	1589 <sup>+807</sup> <sub>-453</sub>	4.22
3C 362	[O III] $\lambda$ 5007	1.6442	2.2839	5.35 $\pm$ 0.28	587	1397 <sup>+71</sup> <sub>-100</sub>	2.78
	H $\beta$	1.5954	2.2820	0.42 $\pm$ 0.25	38	766 <sup>+1439</sup> <sub>-376</sub>	3.33
	He II $\lambda$ 4686	1.5388	...	0.40 $\pm$ 0.44	29	...	4.11
	[Ne III] $\lambda$ 3869	1.2705	...	0.02 $\pm$ 0.52	2	...	4.25
	[O II] $\lambda$ 3727	1.2221	2.2790	1.23 $\pm$ 0.34	101	1099 <sup>+368</sup> <sub>-247</sub>	3.71
4C +40.36	[O III] $\lambda$ 5007	1.6360	2.2675	35.29 $\pm$ 0.59	832	1987 <sup>+28</sup> <sub>-52</sub>	12.98
	H $\beta$	1.5905	2.2720	3.24 $\pm$ 0.48	74	1723 <sup>+289</sup> <sub>-228</sub>	13.33
	He II $\lambda$ 4686	1.5328	2.2709	0.76 $\pm$ 0.61	17	1823 <sup>+5541</sup> <sub>-1126</sub>	13.91
	[Ne III] $\lambda$ 3869	1.2640	2.2670	3.10 $\pm$ 0.81	89	1741 <sup>+594</sup> <sub>-378</sub>	10.64
	[O II] $\lambda$ 3727	1.2179	2.2677	13.89 $\pm$ 0.73	406	2390 <sup>+151</sup> <sub>-139</sub>	10.47
4C +48.48	[O III] $\lambda$ 5007	1.6749	2.3452	15.57 $\pm$ 0.21	978	1243 <sup>+29</sup> <sub>-10</sub>	4.76
	H $\beta$	1.6246	2.3422	1.96 $\pm$ 0.28	111	1795 <sup>+269</sup> <sub>-222</sub>	5.28
	He II $\lambda$ 4686	1.5676	...	0.47 $\pm$ 0.20	25	...	5.60
	[Ne III] $\lambda$ 3869	1.2953	2.3479	0.83 $\pm$ 0.22	44	1044 <sup>+425</sup> <sub>-223</sub>	5.58
	[O II] $\lambda$ 3727	1.2473	2.3467	3.98 $\pm$ 0.24	232	1693 <sup>+122</sup> <sub>-111</sub>	5.12
MRC 2104-242	[O III] $\lambda$ 5007	1.7469	2.4889	5.73 $\pm$ 0.18	2486	1220 <sup>+52</sup> <sub>-45</sub>	0.66
	H $\beta$	1.6968	2.4907	0.88 $\pm$ 0.23	307	1423 <sup>+746</sup> <sub>-423</sub>	0.82
	He II $\lambda$ 4686	1.6349	...	0.23 $\pm$ 0.22	76	...	0.87
	[O II] $\lambda$ 3727	1.3012	2.4913	0.97 $\pm$ 0.22	1459	1982 <sup>+809</sup> <sub>-514</sub>	0.19
	[Ne V] $\lambda$ 3426	1.1953	...	0.14 $\pm$ 0.25	... <sup>g</sup>	...	... <sup>g</sup>
4C +23.56	[O III] $\lambda$ 5007	1.7440	2.4832	7.33 $\pm$ 0.58	474	1258 <sup>+105</sup> <sub>-122</sub>	4.44
	H $\beta$	1.6985	2.4941	1.88 $\pm$ 0.96	102	3047 <sup>+2989</sup> <sub>-1130</sub>	5.27

TABLE 2—*Continued*

Common Name	Lines	Wavelength ( $\mu\text{m}$ )	Redshift <sup>a</sup>	Line Flux <sup>b</sup>	Equivalent Width <sup>c</sup> ( $\text{\AA}$ )	FWHM <sup>a,d</sup> ( $\text{km s}^{-1}$ )	Continuum Level <sup>e</sup>
	He II $\lambda 4686$	1.6322	...	$0.90 \pm 0.70$	44	...	5.93
	[O II] $\lambda 3727$	1.2982	...	$1.47 \pm 0.74$	69	...	6.13

<sup>a</sup>For faint emission lines represented by an ellipsis, we assume that the redshift is the same as that for [O III]  $\lambda 5007$  and that the FWHM is the instrumental value of  $\sim 75 \text{ \AA}$ .

<sup>b</sup>The flux with  $1 \sigma$  errors, in units of  $10^{-16} \text{ erg s}^{-1} \text{ cm}^{-2}$ .

<sup>c</sup>The rest-frame equivalent width. The signal-to-noise ratios are almost the same as that of the flux.

<sup>d</sup>No correction has been made for the instrumental width of  $\sim 75 \text{ \AA}$ , which corresponds to  $\sim 1400 \text{ km s}^{-1}$  at  $1.60 \mu\text{m}$  and  $\sim 1800 \text{ km s}^{-1}$  at  $1.25 \mu\text{m}$ . Note that the typical seeing size ( $\sim 0''.7$ ) is smaller than the slit width ( $1''$ ), causing smaller line width than the instrumental value.

<sup>e</sup>The flux density of the continuum at the line position in units of  $10^{-15} \text{ erg s}^{-1} \text{ cm}^{-2} \mu\text{m}^{-1}$ .

<sup>f</sup>The average redshift for  $\text{H}\gamma$  and [O III]  $\lambda 4363$ .

<sup>g</sup>The continuum level becomes a negative value.

TABLE 3  
UV LINE FLUX

Common Name	C IV $\lambda 1549^a$	He II $\lambda 1640^a$	C III] $\lambda 1909^a$	Reference
MRC 0200+015	$4.2 \pm 0.5$	$3.2 \pm 0.4$	$4.0 \pm 0.5$	1
TXS 0211–122	$2.82 \pm 0.10$	$1.57 \pm 0.03$	$0.74 \pm 0.05$	2
MRC 0214+183	$3.0 \pm 0.3$	$1.8 \pm 0.2$	$1.8 \pm 0.2$	1
MRC 0406–244	$4.0 \pm 0.3$	$5.4 \pm 0.3$	$4.9 \pm 0.5$	3,4
B3 0731+438	$4.65 \pm 0.10$	$3.04 \pm 0.05$	$2.12 \pm 0.05$	2
TXS 0828+193	$18.17 \pm 0.45$	$10.38 \pm 0.14$	$5.59 \pm 0.68$	2
4C –00.54	$2.91 \pm 0.20$	$2.15 \pm 0.05$	$0.96 \pm 0.07$	2
4C –00.62	$2.7 \pm 0.3$	$1.7 \pm 0.2$	$1.2 \pm 0.2$	1
4C +10.48	$0.2 \pm 0.2$	$0.9 \pm 0.2$	$0.2 \pm 0.1$	1
4C +40.36	$13.61 \pm 0.51$	$7.77 \pm 0.56$	$7.39 \pm 1.18$	2
4C +48.48	$5.55 \pm 0.05$	$5.32 \pm 0.35$	$3.28 \pm 0.10$	2
MRC 2104–242	$2.4 \pm 0.3$	$3.0 \pm 0.3$	$2.1 \pm 0.9$	5,6
4C +23.56	$1.80 \pm 0.15$	$1.50 \pm 0.10$	$1.06 \pm 0.10$	2

<sup>a</sup>The flux with  $1\sigma$  errors, in units of  $10^{-16}$  erg s<sup>-1</sup> cm<sup>-2</sup>.

REFERENCES.—(1) Röttgering et al. 1997; (2) Vernet et al. 2001; (3) Rush et al. 1997; (4) Taniguchi et al. 2001; (5) Villar-Martín et al. 1999; (6) Overzier et al. 2001.

NOTE.—The UV line flux taken from the past literature. The typical slit width is  $1'' - 2''$ , and the spatial extent of the aperture is large enough to cover all the flux of emission lines.

TABLE 4  
BEST FIT PARAMETERS

Common Name	Single-Photoionization Model					Shock+Precursor model		
	$\chi_{\text{ph}}^2$ <sup>a</sup>	$\alpha$	$Z$	$\log U$	$\log N_{\text{H}}$ <sup>b</sup>	$\chi_{\text{s+p}}^2$ <sup>a</sup>	$B/\sqrt{n}$	$v$
MRC 0200+015	2.94	-0.615	0.260	-2.415	2.00	41.8	...	...
TXS 0211-122	30.3	...	...	...	...	6.45	0.245	500 <sup>c</sup>
MRC 0214+183	2.94 <sup>d</sup>	-0.500	0.183	-2.269	3.47	34.6 <sup>d</sup>	...	...
MRC 0406-244	14.2	-1.176	0.530	-2.323	1.00 <sup>c</sup>	115	...	...
B3 0731+438	41.0 <sup>e</sup>	...	...	...	...	154	...	...
TXS 0828+193	117 <sup>e</sup>	...	...	...	...	251	...	...
4C -00.54	2.40	-0.896	3.000 <sup>c</sup>	-1.699	1.00 <sup>c</sup>	1.42	0.013	481
4C -00.62	6.18	-0.172	0.131	-2.070	3.00	7.15	0.637	500 <sup>c</sup>
4C +10.48	4.41	-1.250	1.762	-2.477	2.00	21.2	...	...
4C +40.36	17.4	-0.402	0.278	-2.272	2.00	19.7	...	...
4C +48.48	57.8 <sup>e</sup>	...	...	...	...	162	...	...
MRC 2104-242	2.94	-0.660	0.147	-2.554	4.00 <sup>c</sup>	6.64	0.000 <sup>c</sup>	440
4C +23.56	0.06	-0.566	0.175	-2.283	3.21	26.0	...	...

<sup>a</sup>The  $\chi^2$  value for the best fit parameters of each model, photoionization ( $\chi_{\text{ph}}^2$ ) or shock+precursor ( $\chi_{\text{s+p}}^2$ ), respectively.

<sup>b</sup>The hydrogen density, which is not as sensitive to the emission line ratio compared to the other parameters (see §3.2.1).

<sup>c</sup>Maximum or minimum value of the domain of the parameter.

<sup>d</sup>Degree of freedom is smaller than the others because He II  $\lambda 4686$  was out of the observed range for this object.

<sup>e</sup>The best fit models were rejected for these results.

TABLE 5  
SIGNIFICANCE LEVEL TO REJECT ZERO CORRELATION HYPOTHESIS

Correlating Value	$\log P_{opt}^a$	$\alpha_{opt}^b$	$\log L_{[OIII]}$	$\log FWHM^c$
$\log P_{radio}^d$	0.797(+0.08)	0.355(−0.28)	0.838(−0.06)	0.781(−0.08)
$\log D_{radio}^e$	0.164(−0.39)	<b>0.040(+0.57)</b>	0.214(−0.35)	0.089(−0.47)
$\alpha_{radio}$	0.385(−0.25)	0.521(+0.20)	0.498(−0.20)	0.484(−0.20)
$\log P_{opt}$	...	<b>0.003(−0.75)</b>	0.055(+0.52)	0.871(−0.05)
$\alpha_{opt}$	...	...	0.760(−0.09)	0.558(+0.18)
$\log L_{[OIII]}$	...	...	...	0.173(+0.39)

<sup>a</sup>Continuum brightness at the position of [O III]  $\lambda 5007$  emission line.

<sup>b</sup>Continuum slope between [O II]  $\lambda 3727$  and [O III]  $\lambda 5007$  (see Figure 1). MRC 2104–242 is not included in this column because the observed  $J$ -band continuum is too faint to determine the reliable color.

<sup>c</sup>FWHM of [O III] emission line without correction of the instrumental width.

<sup>d</sup>Radio power at rest-178 MHz, interpolated from the observed-408 MHz and 1.4 GHz fluxes.

<sup>e</sup>Radio size (Carilli et al. 1997; Pentericci et al. 1999, 2000).

NOTE.—The significance level at which the null hypothesis of zero correlation is disproved. Smaller value indicates a significant correlation (bold values). Values in parentheses are the correlation coefficients. MRC 0156–252 is not included in these calculations because this object is expected to be a dusty quasar, showing different characteristics from the other sample (see Appendix A.1.).

This figure "fig6.gif" is available in "gif" format from:

<http://arxiv.org/ps/astro-ph/0308062v2>